Effect of Temperature on The Kinetics of Electrochemical Insertion of Li-Ions into a Graphite Electrode Studied by Kinetic Monte Carlo

E. M. Gavilán-Arriazu,[1,2,z] M. P. Mercer,[3,4,5] O. A. Pinto,[2] O. A. Oviedo,[1] D. E. Barraco,[6] H. E. Hoster,[3,4,5] and E. P. M. Leiva[1,z]

[1]*Departamento de Química Teórica y Computacional, Facultad de Ciencias Químicas, Universidad Nacional de Córdoba, INFIQC, Córdoba, Argentina*
[2]*Instituto de Bionanotecnología del NOA (INBIONATEC). Universidad Nacional de Santiago del Estero (UNSE), G4206XCP Santiago del Estero, Argentina*
[3]*Department of Chemistry, Lancaster University, Bailrigg, Lancaster, United Kingdom*
[4]*ALISTORE European Research Institute CNRS FR 3104, Hub de l'Energie, 80039 Amiens, France*
[5]*The Faraday Institution, Harwell Science and Innovation Campus, Didcot, United Kingdom*
[6]*Facultad de Matemática, Astronomía y Física, IFEG-CONICET, Universidad Nacional de Córdoba, Córdoba, Argentina*

The effect of temperature on the kinetics of electrochemical insertion/removal of lithium in graphite is analyzed by kinetic Monte Carlo methods. Different electrochemical techniques are simulated at different temperatures and responses are compared with experimental results. Simulated voltammograms show, similarly to experiment, how the behavior of the system becomes closer to equilibrium as temperature increases. Calculated chronoamperometric profiles show a different qualitative behavior in the current at different temperatures, especially in the Cottrell representation peaks, explained in terms of the relative importance of diffusive versus charge transfer processes at different temperatures. Results at room temperature are in good agreement with experiment, and we further evaluate trends at elevated temperature that have not yet been described in experimental or theoretical works. Exchange current densities for different degrees of lithium intercalation at different temperatures are predicted using potentiostatic simulations, showing an Arrhenius-type relationship. The dependence of the exchange current on electrolyte composition is simulated by investigating the effect of different activation energy barriers at different temperatures. The influence of temperature on diffusion coefficients as a function of lithiation fraction in graphite is simulated and related to Arrhenius plots, explaining the experimentally observed changes in diffusion phenomena with lithium composition and temperature.

 [DOI: 10.1149/2.0332001JES]

Manuscript submitted September 30, 2019; revised manuscript received December 4, 2019. Published December 19, 2019. *This paper is part of the JES Focus Issue on Mathematical Modeling of Electrochemical Systems at Multiple Scales in Honor of Richard Alkire.*

Li-ion batteries designed with graphite anodes are still the most used in small electronic devices and electric vehicle applications. The intercalation process of Li-ion in graphite involves the appearance of different lithium-graphite intercalation compounds (LGIC), commonly referred to as "stage n" in the literature, where n denotes an integer number that describes the number of graphene layers between two lithium-ion occupied sheets. Understanding the impact of external variables, such as pressure or temperature in batteries is crucial to improve their functionality, i.e. their cyclability, lifetime, charging time, to name just a few of these variables. In particular, the critical importance of temperature for the performance of the anode has been recently appreciated, concerning the formation and stability of the solid electrolyte interphase (SEI), the onset of lithium plating, and interfacial resistances. A full understanding of the kinetic processes governing the staging transitions has remained elusive so far. Investigating and modelling the dependence of these processes on temperature provides additional validation to grasp the relative importance of the different physical mechanisms on different length and time scales, potentially allowing a predictive capability in cell level models.

The consequences of temperature changes for graphite anodes in Li-ion batteries have been the topic of different investigations. A significant work was done by Dahn,[1] who obtained the phase diagram for the lithium/graphite electrochemical cell after analyzing X-Ray diffraction patterns. Levi et al.[2] studied temperature effects on kinetics and thermodynamics for the electrochemical insertion of lithium ions in graphite. The cited works showed how lithium (de)intercalation is affected by applying different potentiostatic steps and cyclic voltammetric transients to obtain the transitions between different stages, transferring between potentials with and without phase coexistence.

They monitored in particular in chronoamperometric experiments, the changes in the product of the current by the square root of time, say $It^{1/2}$, as a function of the logarithm of time , saylog(t). Since the product $It^{1/2}$ stems from normalization of the current by the Cottrell diffusion current,[3] we will denote the $It^{1/2}$ vs log(t) plots as the "Cottrell representation" of the potentiostatic transients. This type of plot showed a maximum that raised as temperature was increased.[2] Ecker et al.[4] and Smart and Ratnakumar,[5] reported that the logarithm of the exchange current density is proportional to the inverse of temperature, but no details were given about exchange current density changes for different states of charge. However, the exchange current density at room temperature for different lithium compositions was reported.[4,6,7] The charge transfer resistance is by definition inversely proportional to the exchange current density, thus experimentally reported charge transfer resistances[8–10] can be used to compare with exchange current densities from simulation results. The influence of solvent composition on charge transfer resistance and/or exchange current density is analyzed in Reference 9.

Lithium-ion diffusion within graphite has been studied in several articles,[2,4,11–29] for example, in the work of Levi and Aurbach,[24] where diffusion coefficients were estimated at different Li-ion loadings. The influence of temperature on diffusion coefficients was also studied.[2,4,20,22] The relationship between rate parameters and temperature for Li-ion graphite systems has been described by the Arrhenius law, as has been observed experimentally.[4,5,8–10,20]

Generally speaking, kinetic Monte Carlo simulations[30] have been demonstrated as an efficient tool to research on the (de)intercalation of lithium in graphite.[16,17,31,32] Experimentally, (de)intercalation is very slow process, where completion of a voltammetric cycle may take more than a day.[33] The simulations provide the additional advantage that atomic level details as a function of time can be directly

[z]E-mail: maxigavilan@hotmail.com; eze_leiva@yahoo.com

visualized, thereby providing information on the atomistic underpinnings of the different trends and features that are observed. Alternative modelling techniques, such as phase field models,[34–36] can allow longer length and time scales to become accessible. As discussed in the literature, this methodology has proved to have a great potential for the simulation of electrochemical reactions at active material/electrolyte interfaces.[37,38] Furthermore, as shown by Roder et al.,[39,40] the coupling of kMC with continuum models is challenging but has great potential to approach simulations to the experimental scale.

In a previous work[41] we tackled the simulation of the kinetics of the Li-ion/graphite system, in an electrochemical scheme, by using kinetic Monte Carlo simulations (kMC). Our previous study also highlighted the potential of kMC as a tool to understand and predict, with atomistic detail, the results arising from the application of different electrochemical techniques commonly used in the laboratory. There, we explained the differences found between the intercalation and deintercalation responses, arising from the application of potentiostatic steps and linear potential sweeps. The results were explained in terms of lithium accumulation inside graphite, next to the interface where the Li-ions are inserted. The behavior of the exchange current density as a function of Li-ion composition was also predicted. Kinetic effects were found to play a fundamental role, requiring a proper description of diffusive phenomena, taking into account the interactions between inserted particles. Another important outcome of that work was to make a link between the theoretical predictions of Montella[42] for the response of potentiostatic steps and the experimental results from Refs. 43,44. After a validation of the kMC procedure by comparison with the results of Ref. 42, the $it^{1/2}$ vs $log\ t$ response was calculated and compared with the results of Levi et al.[43,44] The simulations presented the same behavior as the experiments: two peaks in potentiostatic steps into potentials involving stage coexistence and only one peak at potentials where only one stage is formed. These features were explained in terms of an atomistic analysis.

Some of the features of this previous modelling are briefly revisited in the Supplementary Material Sections: cyclic voltammetry, the calculation of diffusion coefficients, model validation and exchange current density results are presented there. In another contribution,[45] kMC and equilibrium Monte Carlo (MC) methods also allowed us to predict the role of kinetics in the formation of the Daumas-Hérold structures in Li-ion graphite intercalation compounds.[46] The occurrence of these types of structures has also been confirmed theoretically by Guo et al. in previous work[36] and very recently by phase-field formulations.[34] In this respect, it is also worth mentioning the use of Maxwell-Cattaneo-Vernotte theory by Maiza et al.[47] to solve the causality issues related to Fickean approaches and capturing structuration of lithium in graphite.

In the present work we tackle the effect of temperature on the electrochemical response of the Li-ion/graphite system using different techniques and analyze the corresponding changes in the exchange current density by kMC simulations. Simulation results are compared with experimental ones and predictions are made for measurements not yet performed. Monte Carlo equilibrium simulations are employed to compare kinetic results with the equilibrium situation.

Model and Computational Details

In order to mimic the graphite substrate, we used a simulation cell consisting of a stack of two-dimensional lattice-gas nets with triangular geometry. The total number of sites is $M = N_x \times N_y \times N_z$, where N_x,N_y and N_z are the number of lateral lattice sites along the x, y and z directions respectively. The two-dimensional lattices are parallel to the x-y plane, while the z direction is perpendicular to this plane, so that the number of planes is given by N_z. The lattice geometry was built using the parameters of the graphite crystalline structure. Hence, each lattice site is located in the center of the carbon hexagons and at half the distance between two adjacent graphene layers.

In order to emulate real events in a graphite anode, we defined certain events and placed limitations to the kMC system in the grand canonical scheme, as shown in (Figure 1): *(i)* ions can be intercalated or deintercalated only on the left side of the simulation box (event *a*); *(ii)* Li-ion diffusion is confined to the right side of the simulation box by a hard wall (event *b*); *(iii)* diffusion is allowed only into empty first neighbors (event *c*); *(iv)* no interlayer particles jumps are allowed (event d), due to the high energy barrier involved, as reported in Ref. 48; *(v)* periodic boundary conditions are set up along the x axis, where the ions are free to move. The system is also periodic in the z direction. The restricted diffusion conditions on the right hand side of the simulation box, due to the imposition of a hard boundary, mimics finite size effects in the material and determines a thickness L_y in the y direction. As discussed in Reference 42, the situation is equivalent to analyzing linear diffusion in a material foil of thickness 2 L_y, symmetrically submitted to insertion on both sides.

In the case of grand canonical Monte Carlo (GCMC) simulations, these only involve attempts to change the occupation state of a given site at the Monte Carlo steps, as these simulations are used to achieve the equilibrium state.

The Hamiltonian that rules particle-particle interactions contains different energy terms. It is inspired in the ansatz by Derosa et al.,[49] has been previously applied in other contributions[45,50,51] and involves a sum over all M lattice sites, as stated in Equation 1. The first summation corresponds to the interaction energy between ions in the same layer, the second is the interaction between ions in different layers and the last one is an occupational term.

$$H = \sum_{i}^{M}\sum_{j\neq i}^{N_{ip}} \frac{c_i c_j \varepsilon}{2}\left[\left(\frac{r_m}{r_{ij}}\right)^{12} - 2\left(\frac{r_m}{r_{ij}}\right)^{6}\right] + \sum_{i}^{M}\sum_{j}^{N_{op}} \frac{c_i c_j \kappa}{2}\left(\frac{r_b}{r_{ij}}\right)^{\alpha} + (\gamma - \mu)\sum_{i}^{M} c_i \qquad [1]$$

where M is the total number of lattice sites, N_{ip} and N_{op} are the number of neighbors in the same and in different layers, respectively. ε denotes the potential energy depth at distance r_m, κ and r_b rule the repulsive interaction and α determines the range of this repulsion. γ denotes an energy parameter used to fit isotherm position, μ is the chemical potential (proportional to electrode potential E vs Li / Li^+, as $\mu = -eE$), r_{ij} is the distance between sites i and j and c is an occupational

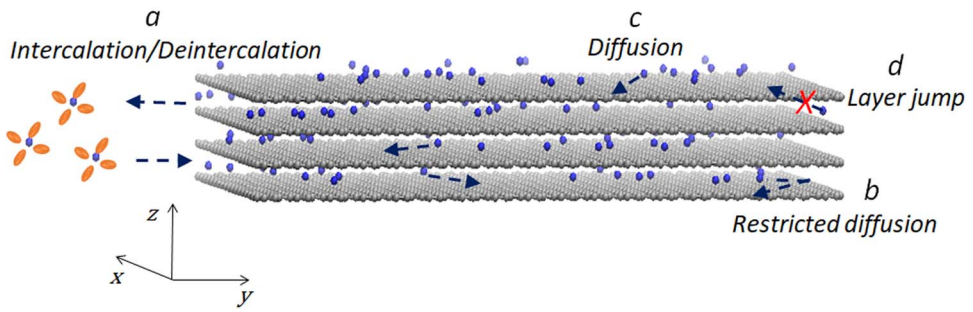

Figure 1. Events and restrictions imposed to the system. Li-ions are represented in blue, graphite in gray, solvated Li-ion are represented with blue spheres surrounded by orange balloons.

Table I. Parameters introduced in the Hamiltonian of Equation 1.

ε [eV]	r_m [Å]	κ [eV]	r_b [Å]	α	γ [eV]
0.0255	4.26	0.255	1.42	4	−0.03

variable for each site ($0 \equiv empty, 1 \equiv full$). The cutoff distances used were 10.0 Å in the x-y plane and 6.0 Å along the z-axis. This yields $N_{ip} = 60$ and $N_{op} = 182$. The present cutoff distances are essentially the same as those used in a previous work[52] and were chosen so as to fit the experimental insertion isotherm. The order of magnitude of the values used is similar to that found in the literature for the screening response of graphite to a single intercalant atom.[53] The sum in the last term of Equation 1 fulfills the condition $\sum_i^M c_i = N_{occ}$, where N_{occ} is the number of graphite lattice sites occupied by Li^+ ions. It is also useful to define a Li-ion concentration as $x = 3N_{occ}/M$, where number 3 was added because the maximum state of charge for lithium inside graphite is one third of the total intercalation sites. The importance of considering coulombic repulsive interaction between lithium ions from different interlayers to determine the staging phenomena has been discussed by Márquez et al.[26]

The values of the parameters used in the Hamiltonian from Equation 1 are summarized in Table I.

The rate equation for the events allowed in the present simulations is given by:

$$\Gamma = \nu_0 \exp\left[-\frac{\Delta^*{}_\sigma + \alpha_{BV}\,(H_F - H_I)}{k_B T}\right] \qquad [2]$$

where ν_0 is a pre-exponential factor, H_I and H_F are the Hamiltonians for the initial and final state respectively, k_B denotes the Boltzmann constant, and T is the absolute temperature. $\Delta^*{}_\sigma$ is the energy barrier for event σ ($\sigma = diff$ for diffusion and $\sigma = i/d$ for insertion/deletion) and $\alpha_{BV} = 1/2$ is the symmetry factor for charge transfer. This proposal involves merging the Arrhenius rate equation with the electrochemical Butler-Volmer equation, and it has been described and applied in References 54,55. The constants in the rate Equation 2 were fitted to experimental results from literature, and were the same values as those used in previous work.[41,45] A value $\nu_0 = 1 \times 10^{13} s^{-1}$ was taken from References 13,17. The diffusion barrier $\Delta^*{}_{diff} = 0.370$ eV, was fitted using the random walk theory and kMC simulations in the canonical ensemble for a single particle, e.g. emulation of the experimental results in the limit of low Li occupation.[24] For 1 M $LiPF_6$-ethylene carbonate (EC)/ diethylene carbonate (DEC) (1:1) as a solvent, a value of $\Delta^*{}_{i/d} = 0.655$ eV was obtained to fit the experimental exchange current density at stage II,[6] and it is close to the energy barriers measured in several other works.[8–10] Other $\Delta^*{}_{i/d}$ values will be used to emulate different solvents, which will be detailed later. The assumption of a temperature-independent value for $\Delta^*{}_{i/d}$ (or a constant preexponential factor) corresponds with the usual assumption of neglecting entropic factors for the calculation of rates in kinetic Monte Carlo simulations.[16]

According to Equation 2, the activation barrier for the event σ is

$$E_{a,\sigma} = \Delta^*{}_\sigma + \alpha_{BV}\,(H_F - H_I) \qquad [3]$$

To perform kMC simulations the rejection-free KMC algorithm was applied.[56] GCMC simulations proceeded, employing the Metropolis algorithm,[57] 1×10^7 Monte Carlo steps (MCS) were used in the equilibration step and in the averaging step respectively.

Linear potential sweep profiles were obtained introducing the following steps into the kMC code:

i. A potential sweep rate, ν, and a potential window $\Delta E_T = E_f - E_0$ were chosen, where E_0 and E_f are the initial and the final potential respectively.
ii. After each kMC event, the potential was increased in $\Delta E_{i+1} = \nu.\Delta t_i$, where Δt_i is the time increment calculated within the usual kMC scheme at time t_i.

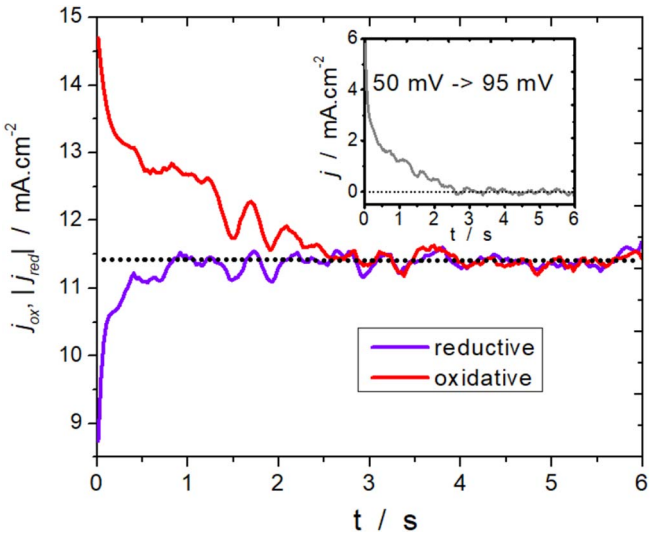

Figure 2. kMC chronoamperometric response to a potential step. The current densities for oxidation and reduction (absolute value) are shown versus time, the exchange current is marked with dotted line. In the inset the net current density vs time is represented.

iii. The potential was modified as $E_{i+1} = E_i + \Delta E_{i+1}$.
iv. When the potential reached the final value (E_f), the scan direction was reversed $E_{i+1} = E_f - \Delta E_{i+1}$.
v. The algorithm finished when the potential reached the initial value E_0.

Since the simulations are very demanding computationally, cyclic voltammograms were simulated using relatively small system sizes, such as $M = 24 \times 24 \times 4$. A potential window from $E_0 = 130$ mV to $E_f = 55$ mVwas selected. Voltammetric profiles at T = 296 K for different potential sweep rates are shown in Figure S1 of the Supplementary Material. Voltammograms at $\nu = 5.0$ mV. s^{-1} were performed at different temperatures.

To perform potentiostatic step simulations, a sample configuration was chosen after the system had reached the steady state at the initial potential. Then, the potential was switched to the final value and the simulation proceeded. The system size used was $M = 24 \times 108 \times 4$.

The exchange current i_0 was obtained from potentiostatic simulations, after the system reached a steady state at a given electrode potential. Under such conditions, the net current became zero, since the oxidative current i_{ox} was equal to the reductive current $|i_{red}|$, $i_{ox} = |i_{red}| = i_0$. That is, the number of inserted and deinserted ions per unit time became the same, as shown in Figure 2. The steady state condition was evaluated by the analysis of a Flyvbjerg-Petersen Plot.[58] From i_0, the exchange current density j_0 was calculated as the exchange i_0 current per unit of area $A_{xz} = L_x \times L_z$.

Chemical diffusion coefficients were calculated using Equations 4 and 5 given below, as was explained in more detail in Section S2 of the Supplementary Material,

$$D_{ch} = \left(\frac{\partial(\mu/k_B T)}{\partial \ln x}\right)_T D_j \qquad [4]$$

$$\Theta = \left(\frac{\partial\,(\mu/k_B T)}{\partial \ln x}\right)_T \qquad [5]$$

where D_j is the jump diffusion coefficient and Θ is the thermodynamic factor. Since the latter is difficult to obtain for x close to phase transitions,[18,59] we have calculated it from the voltammetric isotherms at the lowest sweep rate. It offers the advantage that it is the same choice as that made in Reference 24 to calculate the D_{ch} from experimental data, so that the present results may be compared with theirs. D_j was calculated in canonical kMC simulations runs starting from

steady-state configurations as follows:

$$D_j = \langle \Gamma_{diff} \rangle \lambda^2/(2d) \quad [6]$$

where Γ_{diff} is the value of the jump rate, $d = 2$ is the system dimension and $\lambda = 2.46$ Å is the characteristic (first neighbors) jump distance.

We neglect the effects of quantum tunneling in the transport of Li through graphite, since these effects are expected to be negligible under the present conditions.

To perform statistics, 40 simulations were carried out for potentiostatic step transients and the figures were smoothed with Chebyshev polynomials for a better representation. In the case of cyclic voltammetry simulations, a series of 40 different runs were used and Chebyshev polynomials were also employed to smooth the curves. In the case of diffusion coefficients and exchange current densities, the averages were taken over 50 and 40 simulation runs respectively.

Results and Discussion

Cyclic voltammetry.—Voltammograms for different temperatures are shown in Figure 3a. In all cases, the presence of two oxidation current peaks i_{po1} and i_{po2}, and of two reduction current peaks i_{pr1} and i_{pr2} can be observed. We label the corresponding peak potentials E_{po1}, E_{po2}, E_{pr1} and E_{pr2}. The snapshots of the simulations for the different processes reveal that the transition $II \leftrightarrow I$ occurs at peak 1, while the transition $Id \leftrightarrow II$ is found at peak 2. The potential peak differences $|E_{po1} - E_{pr1}|$ and $|E_{po2} - E_{pr2}|$ reveal hysteresis in all cases.

The increase in the temperature of the system causes a shift of the simulated oxidation peaks toward more negative potentials, while the opposite occurs with the reduction peaks, which are shifted toward more positive potential values. The result shows that the peak separation on the forward and reverse scans $|E_{po1} - E_{pr1}|$ and $|E_{po2} - E_{pr2}|$ decreases as temperature increases, indicating hysteresis is reduced by an increase in temperature. On the other hand, the half width of the peaks increases as temperature does so.

The hysteresis phenomenon at different temperatures can be observed in the isotherms constructed from Figure 3 and shown in Figure 4.

All isotherms show a hysteresis loop between the intercalation and deintercalation sweeps. The direction of the shift is illustrated in Figure 4a, which corresponds to T = 296 K. Analysis of these three figures shows that as temperature increases, from Figures 4a to 4c, the hysteresis loop is progressively reduced, as emphasized by the black arrows. This behavior is expected if we note that, when the temperature rises, the activation barrier for Li-ion exchange can be surmounted more easily so that the ions can exchange faster across the interphase and the hysteresis becomes reduced. We will return to this point later. The same features have been found in experiments by Levi et al. (Figure 1 from Ref. 2).

It is important to emphasize that the sweeps rates used to simulate the voltammograms are much faster than those employed in experiments. This is so because the graphite sheets used in the simulations are several orders of magnitude smaller than the experimental ones. Note that we expect the simulated temperature trends to apply regardless of particle size. Tao et al.[60] have recently characterized individual $LiMn_2O_4$ (LMO) particles by scanning electrochemical cell microscopy (SECCM). They showed that very high potential sweep rates (0.1-10 mV.s^{-1}) during lithium (de)intercalation still yield well resolved features in the voltammograms. As highlighted there, these sweep rates are 2–4 orders of magnitude greater than the ones used to characterize LMO or graphite in a form used in commercial electrodes, in which there is a wider particle size distribution, and in which one must account for porosity of the electrode structure. Although to the best of our knowledge, comparable experiments have not yet been performed with smaller graphite crystallites, we would expect something similar to occur in that case. We therefore emphasize the need for further systematically controlled particle size experiments on graphite to bridge the gap in length and time scales.

Figures 3b and 3c show a comparison between the simulated peak potentials of the anodic and cathodic process related to the $I \leftrightarrow II$ transition and the experimental results. As marked above, the experimental results show a larger peak shift at all temperatures than the simulations, probably due to the inherently larger average particle size in the experiments. While the latter are typically 6 μm thick,[61] the thickness of the simulated slabs is about 0.0051 μm. However, the simulated results resemble the relative shifts with temperature found experimentally.

Potentiostatic steps.—The kinetics of the intercalation/deintercalation phenomenon can be analyzed in further detail from chronoamperometric profiles. We have validated the present model by comparing its predictions with theoretical results from Montella,[42] who assumed linear diffusion and Langmuirian insertion reaction kinetics to calculate potentiostatic transients. The equivalence between the present model in the limit of non-interacting inserted ions and that of Montella is briefly discussed in Section S3 from Supplementary Material. Hence, it is here relevant to begin

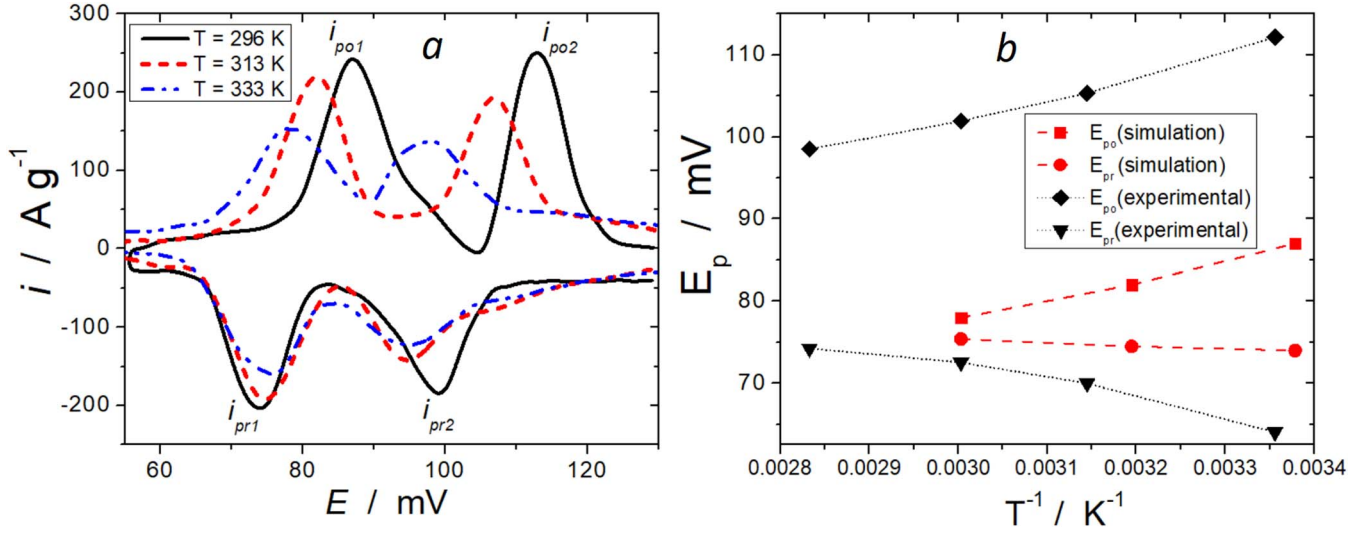

Figure 3. Effect of temperature on simulated voltammetric profiles. a) Voltammograms at $v = 5.00$ mV.s^{-1} and for different temperatures. b) E_{p1} vs T^{-1} for voltammetric data from the simulations shown in Figure 3a (red dashed lines, the symbols are different for oxidation and reduction). E_{p1} vs T^{-1} from experimental data, taken from Fig. 1 from Ref. 2 (black solid lines, the symbols are different for oxidation and reduction). On Figure b the error bars for the simulated data are smaller than symbol size.

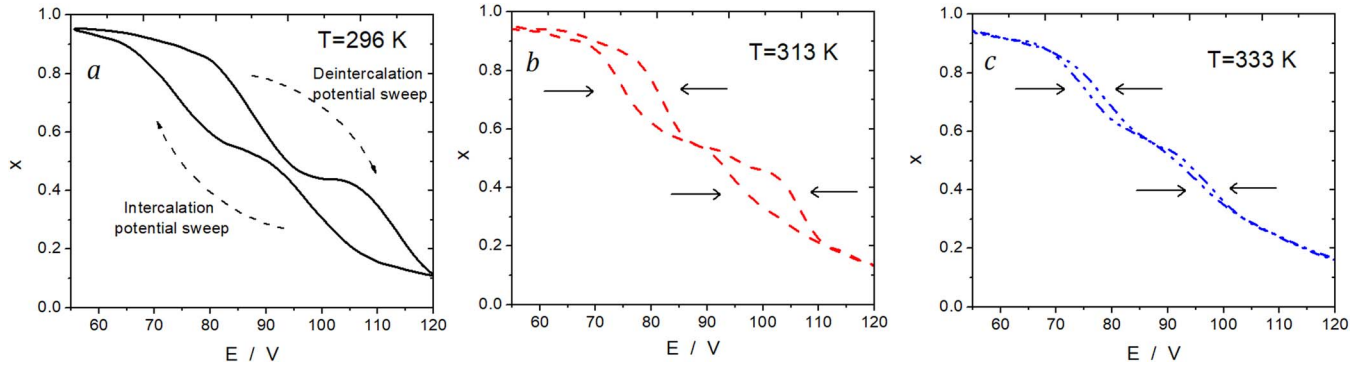

Figure 4. Isotherms at different temperatures, 296 K (a), 313 K (b) and 333 K (c), indicated in each figure, at $v = 5.00$ mV.s^{-1}. These plots were constructed from the voltammograms in Figure 3. For simplicity, the colors and line types are the same as those used in Fig. 3. Black arrows indicate the direction of hysteresis reduction as temperature increases.

with the simulation of the potentiostatic steps under Langmuirian conditions at different temperatures, and then go more deeply into the more complex model that emulates the Li-ion/graphite system, as described by the Hamiltonian in Equation 1.

Within the framework of Montella's modeling, it is relevant to calculate the Cottrell current (I_{Cott}), Equation 7, and the diffusion time constant ($\tau_{0,y,T}$), Equation 8. To do that, the total charge inserted in the potentiostatic step, ΔQ, the box length at the y-axis, L_y and the diffusion coefficient for diluted concentrations, $D_{0,T}$ are introduced in the following equations:

$$I_{Cott} = \frac{\Delta Q}{\sqrt{\pi t \tau_{0,y,T}}} \quad [7]$$

$$\tau_{0,y,T} = \frac{{L_y}^2}{D_{0,T}} \quad [8]$$

The diffusion coefficients at diluted Li-ion compositions $D_{0,T} = D_{x\to 0}$ can be calculated using the random walk theory. So, using an y-axis size for the system $L_y = 153.36$ Å, we obtain the diffusion time constants and diffusion coefficients detailed in Table II.

In Montella's work, the results are assessed for different values of a kinetic dimensionless parameter called Λ. According to the derivation presented in Section S3 of Supplementary Material for our system Λ is given by:

$$\Lambda = \frac{|\Gamma_r d_s|}{D_{0,T}/L_y}, \quad [9]$$

Table II. Parameters used to simulate the transients shown in Figure 5. The parameter Λ was defined in Ref 42 and its evaluation for the present system is discussed in the text.

Temperature, T [K]	Diffusion time constants, $\tau_{0,y,T}$ [s]	$\log D_{0,T}$ [cm^2.s^{-1}]	Λ
296	5.145×10^{-4}	−8.34	1.15
313	2.35×10^{-4}	−8.00	1.43
333	1.03×10^{-4}	−7.64	1.70

where $\Gamma_r = v_0 \exp\left[-\frac{\Delta^*_r + (1/2)(\gamma - \mu)}{k_B T}\right]$ is the rate equation for ion insertion. $d_s = 2.13x10^{-8}$ cm is a distance parameter deduced for the graphite substrate unit cell. The values for Λ are detailed in Table II, assuming an energy barrier for insertion of $\Delta^*_r = 0.425$ eV.

The results of the kMC simulations are presented in Figure 5 for three temperatures $T = 296$ K, 313 K and 333 K. The normalized current (Figure 5a) versus the normalized time shows a large current decrease at the beginning of the potentiostatic steps, which is steeper for higher temperatures, then all currents drop to zero. The current normalized by the Cottrell current versus the logarithm of the normalized time (Figure 5b) presents a single peak in all cases, which becomes higher as temperature increases.

To proceed further with the model given by the Hamiltonian, Equation 1, we need to choose suitable electrode potentials for potentiostatic

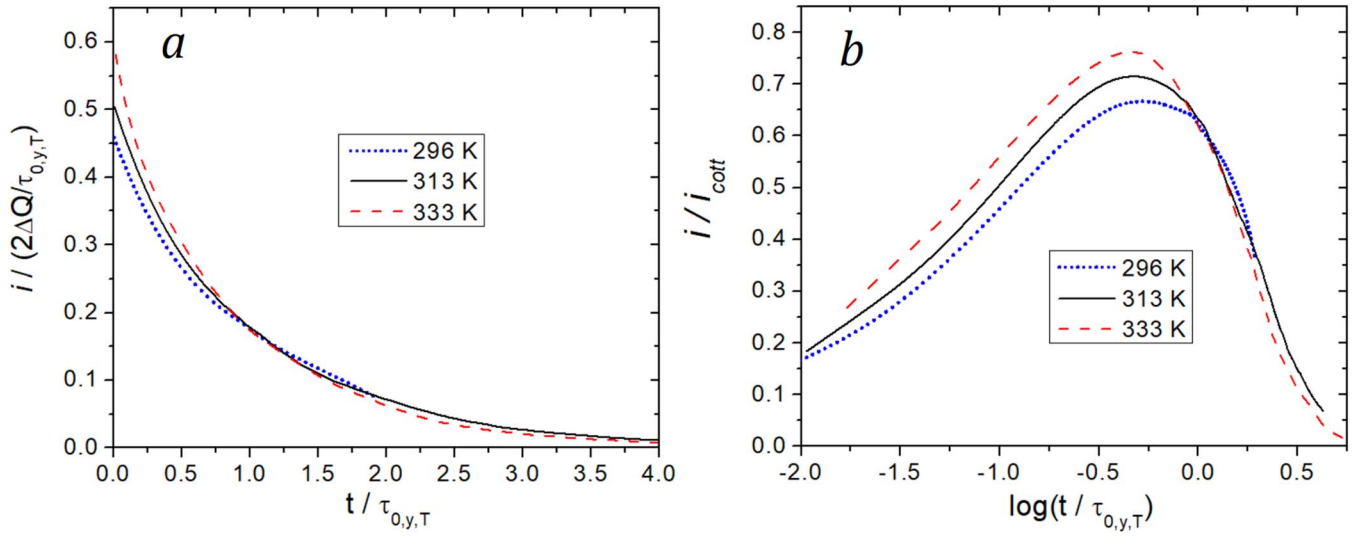

Figure 5. kMC simulations of potentiostatic transients for three different temperatures, emulating the Langmuirian conditions from Reference 42.

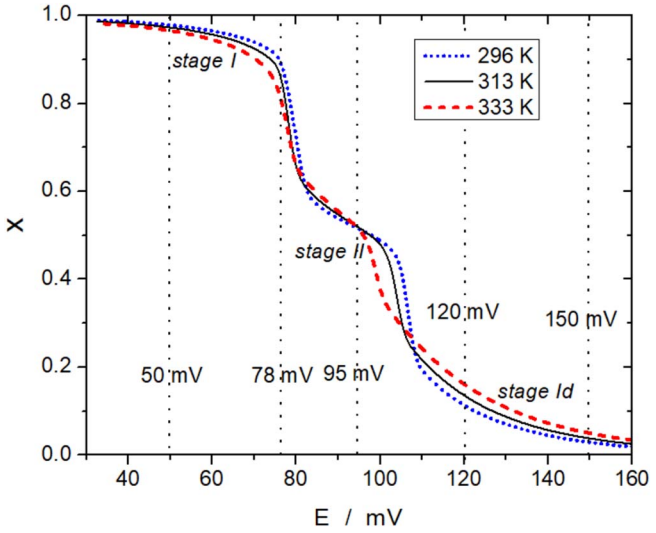

Figure 6. Equilibrium isotherms for Li-ion insertion in graphite at T = 296 K (blue dotted line), 313 K (black line), 333 K (red dashed line). The electrode potentials selected to perform the potentiostatic steps are indicated with vertical dotted black lines. The stages occurring at the plateaus are indicated with italic letters.

step simulations. With this purpose, we simulated GCMC equilibrium isotherms at different temperatures (T = 296 K, 313 K and 333 K) (Figure 6). These isotherms provide a picture of the potential windows where we can find the occurrence of stages and stage transitions. Stages Id, I and II are evident as plateaus in x, as indicated in Figure 6. The potentials selected for potentiostatic steps are indicated there with vertical black dotted lines.

Let us first consider the effect of temperature on a potentiostatic step where no stage coexistence is evident in the present model, say 120 mV → 150 mV. At the potentials involved in this step, only stage Id is formed at all the temperatures analyzed. The kMC results for these transients are shown in Figure 7 in the i/t and $|i|t^{1/2}/\log t$ representations.

Figure 7a shows a faster drop of the current to zero for higher temperatures. The current jump when the potentiostatic step is imposed (immediately after t = 0 s) is also larger for higher temperatures. This behavior denotes that, as temperature is increased, more charge is extracted from the system in a short time. Figure 7b shows a single peak in the $|i|t^{1/2}/\log t$ representation for Li-ion deinsertion in all cases. As in the Langmuirian case analyzed in Figure 6b, the peak maximum is larger and appears at shorter times when temperature increases, but this effect is strongly emphasized. It is remarkable that the results close to room temperature (T = 296 K) (blue curves in Figures 7a and 7b) are very similar to the experimental results observed for the Id-Id potentiostatic steps from Ref. 43.

Next, we analyze two cases of potentiostatic steps where stage coexistence is evident, one for the oxidation process (deintercalation) and the other for reduction (intercalation). In order to study how temperature affects the current responses, particularly in the $|i|t^{1/2}$ vs $\log t$ representation, we focus here on two types of potentiostatic steps where the events are clearly identifiable.

Figure 8 shows results for the 50 mV → 95 mV potentiostatic steps, where the system goes from stage I to II (see Figure 6). The lithium composition responses, x vs t, Figure 8a, reveal that the deintercalation process leading from stage I to II is faster when temperature increases. The times when the system reaches stage II at each temperature are marked with vertical dotted lines, using the same color as in the x vs t curves. The same feature is reflected in the current profiles, Figure 8b, i.e., where the system reaches zero current faster for higher temperature conditions. As in the previous case, this is a consequence of the fact that the activation energy can be overcome more easily. However, in the present simulation, two peaks are evident in the $|i|t^{1/2}$ vs $\log t$ representation, Figure 8c, for all temperatures. The peak at shorter times, p_1, increases faster with temperature, as compared with the second one, p_2. This feature is highlighted with a dashed black arrow. For T = 296 K (blue curve), p_1 is smaller than p_2, for T = 313 K (black curve) both peaks are of comparable height and for T = 333 K (red curve) p_1 becomes higher than p_2.

During the 50 mV → 95 mV potentiostatic step, the system runs through different situations, denoted with i, ii, etc, and indicated by arrows in Figure 8b. These correlate with snapshots from the simulations (Figure 9). The next analysis is valid for all temperatures, although we only concentrate on the description for T = 333 K. Figure 9a shows the system before the application of the potentiostatic step, at t = 0 s, where stage I is evident. This point is marked with (i) in Figures 8b and 8c. When the potentiostatic step is applied there is a fast Li-ion deinsertion from the graphite, between 0 s < t < 0.5 marked with (ii) in Figures 8b and 8c. After that, a portion of stage II is formed at t ≈ 0.5 s (marked with red circle in Figure 9b), this event is marked with (iii) in Figures 8b and 8c. Thus, the origin of the minimum between peaks p_1 and p_2 is the generation of a portion of stage II next to the

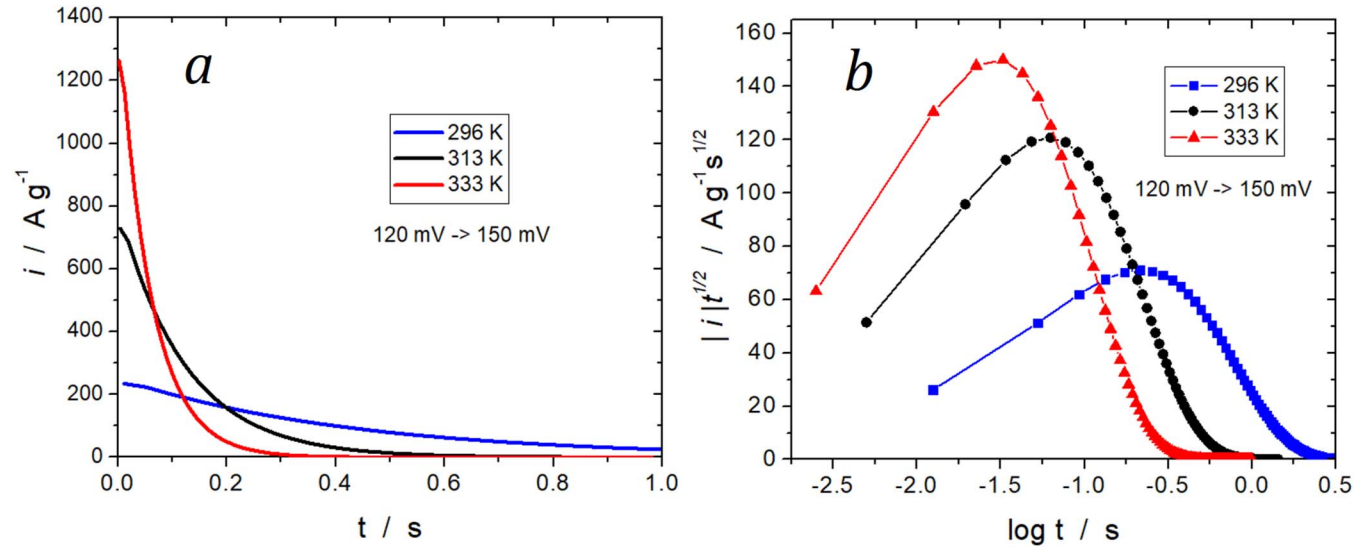

Figure 7. kMC results for a potentiostatic step from 120 mV to 150 mV at the temperatures indicated in the figure. a) chronoamperometric profiles. b) $|i|t^{1/2}$ vs log t representation.

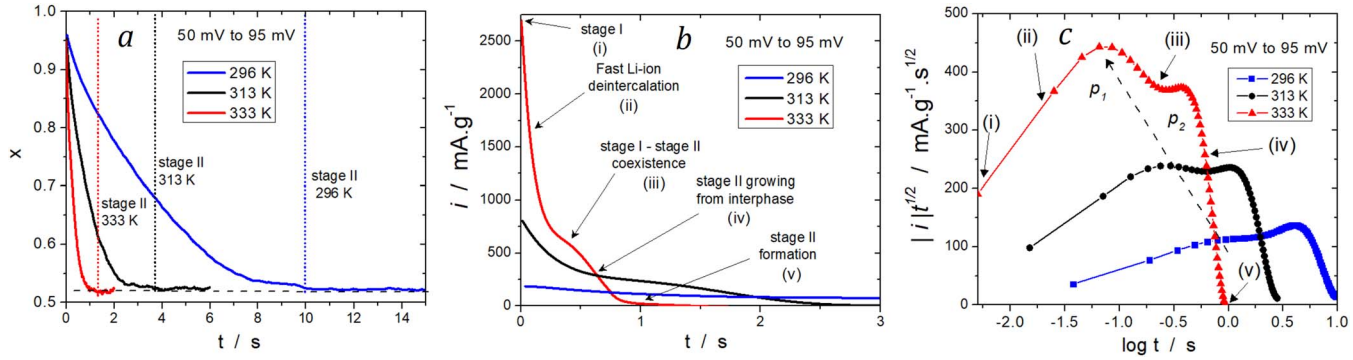

Figure 8. kMC simulations of a potentiostatic step from 50 mV to 95 mV for three different temperatures. a) lithium composition vs t. b) chronoamperometric response. c) $|i|t^{1/2}$ vs log t plots. Features for the different processes are marked with arrows from (i) to (v) in Figs b and Figure c. The denominations of the peaks are only marked for T = 333 K, but the same notation is valid for all temperatures. The different (i) to (v) features may be correlated with simulation snapshots presented in Figure 9.

interphase, due to fast Li-ion deintercalation. Then, after the minimum, between 0.5 s < t < 1 s the portion of stage II expands to the inner part of the electrode (this zone is indicated with (iv) and an arrow in Figures 8b and 8c). The stage growth direction is indicated with a red arrow in Figure 9c. At t ≈ 1 s the system reaches the stage II complete formation (Figure 9d), marked with (v) in Figures 8b and 8c.

Thus, according to the previous analysis, p_1 can be related with the exchange of Li-ion at the interphase when the potentiostatic step is applied. Then, when T increases, the rate of Li-ion deinsertion is larger, since the energy barrier can be surmounted more easily, and p_1 is bigger. Although p_2 seems to rise with temperature, the effect is not as strong as that observed for p_1. This suggests that p_2 does not depend on the rate of Li-ion exchange as p_1 does, or rather, that it does not depend so strongly on temperature. A video of the complete process for 296 K (Li-ion-graphite-Deintercalation.mp4) is available as part of the Supplementary Material.

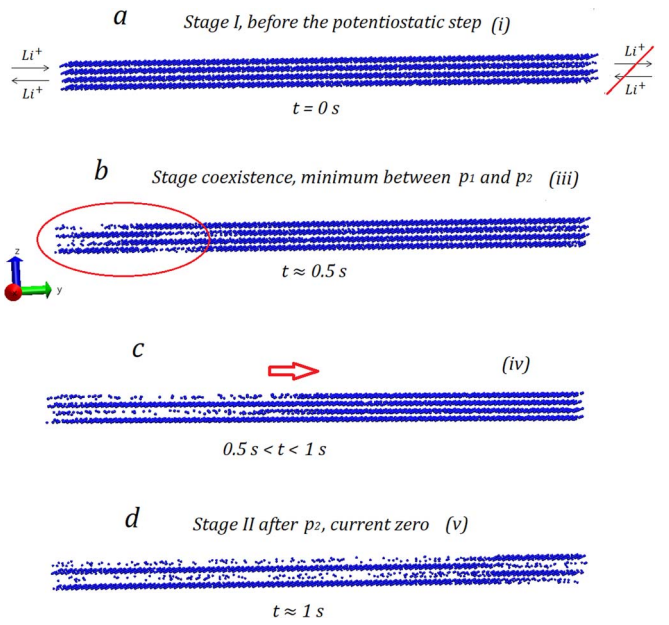

Figure 9. Snapshots taken from kMC simulations for a potentiostatic steps from 50 mV to 95 mV. Li-ions are represented in blue; graphite was omitted with visualization purposes. The graphite/electrolyte interphase (Li-ion exchange) is highlighted on the left of Figure a with arrows, illustrating lithium intercalation / deintercalation. On the right of the figure, lithium ions are confined by a wall and cannot be exchanged with the reservoir of particles. This effect is represented with crossed arrows.

A similar analysis can be done for the potentiostatic step 95 mV → 78 mV, where the system goes from stage II to a mixed stage II-stage I Li-ion arrangement. The events can be clearly observed by looking at the Cotrell $|i|t^{1/2}$ vs $\log t$ representation, Figure 10, where two peaks, separated by a minimum, are evident at all temperatures. Since the current responses are similar to those in the previous cases, they are not shown in Figure 10. They are named like in the previous case: p_1 is the peak that appears at shorter times and p_2 is the peak at longer times for each temperature. As we did before, different regions are labeled in Figure 10 for 313 K. p_1 increases rapidly with temperature, but opposite to the case of the deintercalation potentiostatic step, p_1 is larger than p_2 at room temperature (blue curve, T = 296 K). Another important difference is the behavior of p_2: while p_1 increases with temperature , p_2 decreases. We will return to this point below. However, a feature common to all processes is that they occur at shorter times as temperature increases, something that is expected based on activated processes.

From the snapshots of the simulations for 95 mV → 78 mV (Figure 11), we can establish a correlation between Figure 10 and the main events occurring at T = 313 K. Before the potentiostatic step (t = 0 s), graphite is occupied by a DH stage II structure (Figure 11a), situation (i) in Figure 10. When the potentiostatic step is applied, a significant

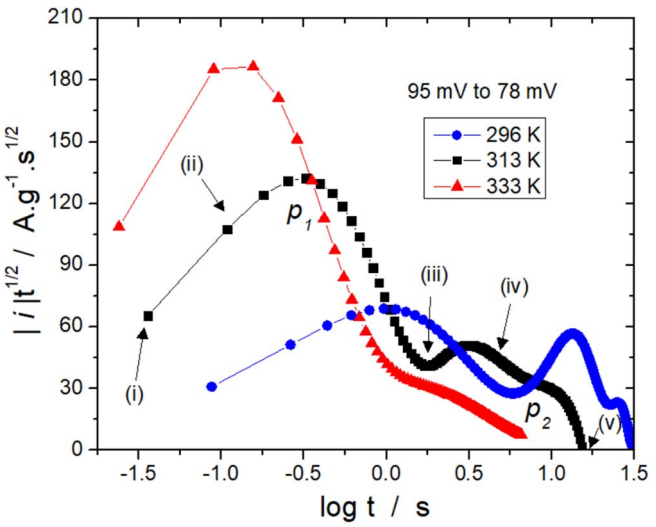

Figure 10. kMC results for the Cottrell representation for a potentiostatic step 95 mV → 78 mV. The main features are pointed with arrows from (i) to (v) for T = 313 K. The peaks p_1 and p_2 are indicated for T = 313 K. The different features may be correlated with simulation snapshots presented in Figure 11.

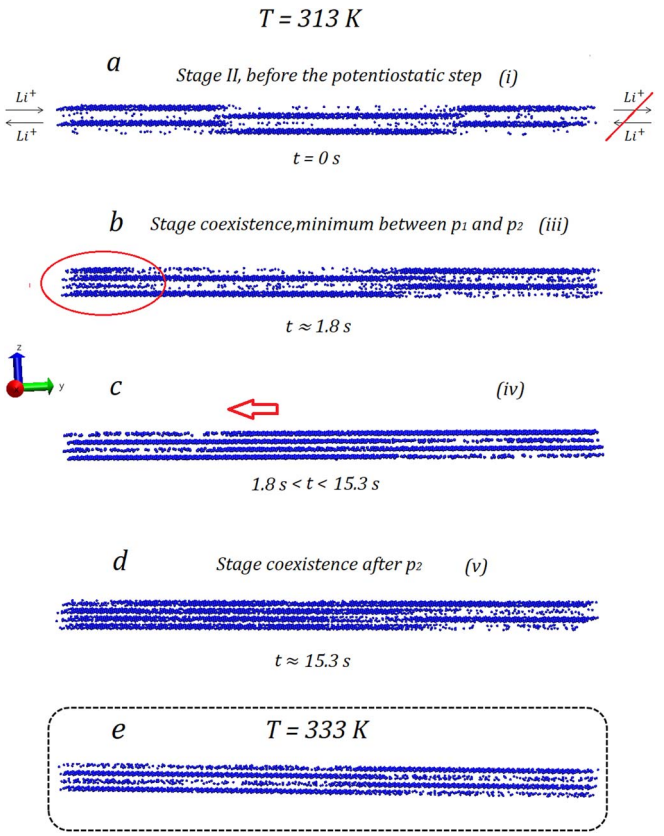

Figure 11. Snapshots for kMC simulations for the potentiostatic step from 95 mV to 78 mV. Li-ion are represented in blue; graphite was omitted with visualization purposes. The graphite / electrolyte interphase (Li-ion exchange) is highlighted in Figure a at the left of the figure with arrows for lithium intercalation / deintercalation. At the right of the figure lithium ions cannot be exchanged with the reservoir of particles, this is represented with crossed arrows. Figures a to d corresponds to T = 313 K. Figure e, enclosed in a dashed line rectangle, is the frame corresponding to the final state of the simulation at T = 333K.

intercalation of Li-ions occurs at the interval 0 s < t < 1.8 s, (ii) in Figure 10, until t ≈ 1.8 s. This time corresponds to a minimum between p_1 and p_2. At this time, a portion of stage I is formed next to the interphase (indicated with a red circle from Figure 11b). This step corresponds to feature (iii) in Figure 10. Thus, the minimum in $|i|t^{1/2}$ vs $\log t$ appears due to a Li-ion nucleation step. A similar behavior has been described for intercalation by Levi et al.[44] Then, at 1.8 s < t < 15.3 s, the portion of stage I disappears and the process continues in a monotonous way incorporating particles, as indicated by the red arrow from Figure 11c. This step corresponds to feature (iv) in Figure 10. At steady state, a mixed stage I-stage II remains in a metastable state after the second peak (Figure 11d, feature (v) from Figure 10). A video of the complete process (Li-ion-graphite-Intercalation.mp4) is available at Supplementary Material. At 333 K the previously described process is slightly different. After the minimum between p_1 and p_2, stage I is eliminated from the system and cannot be found inside graphite. That is, Li-ion is incorporated, but without stage I formation, until the system reaches a configuration like that from Figure 11e.

In summary, the process that is evident in p_1 seems to be controlled by the rate of charge transfer at the interphase, which is given by the activation energy for Li-ion insertion/deinsertion. Thus, as temperature increases, this energy barrier can be surmounted more easily, and a large change in the current is observed at the beginning of the potentiostatic step. On the other hand, p_2 is related to a lower (diffusive) activation barrier and is not affected as strongly as p_1 by temperature changes. This is an indication that the height of p_2 is controlled not

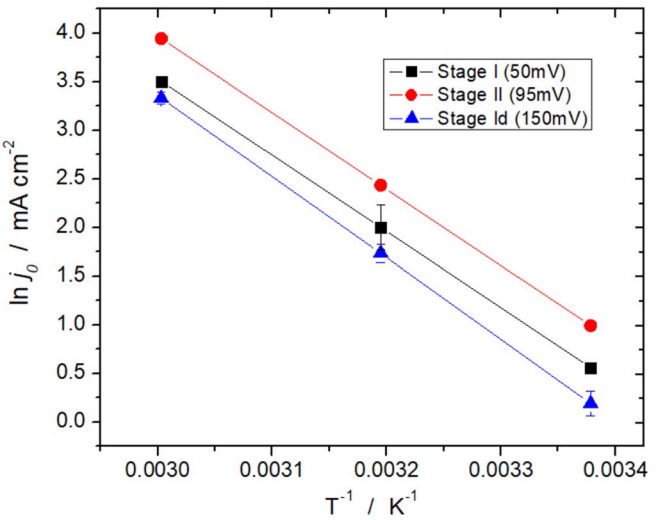

Figure 12. Arrhenius-type plots of the exchange current density for three different stages of Li-ion insertion in graphite. Stage Id is represented in blue triangles, stage II with red circles and stage I with black squares.

only by the charge transfer rate, as p_1 is. In fact, frame analysis revealed that p_2 occurs after the formation of stage coexistence inside graphite, and that the current response is related to the growth of stage I inside graphite. The latter phenomenon is controlled by the diffusion rate. A more detailed explanation on p_1 and p_2 origin can be found in a previous work,[41] and the modification peaks p_1 and p_2, which take place with temperature, confirm the previous statements. Let us now analyze why p_2 decreases, whereas p_1 increases in Figure 10. Looking at the equilibrium isotherms for different temperatures at 78 mV (Figure 6), it can be noted that at a given potential, x is different at all temperatures, being larger for 296 K, smaller for 313 K and the smallest for 333 K. Thus, the values of x that the system can reach at steady state for a potentiostatic step 95 mV → 78 mV, are different for each temperature. In this respect, the 333 K $|i|t^{1/2}$ vs $\log t$ occurrence can be understood as follows: the largest Li-ion insertion takes place at the beginning, at 333 K, generating the biggest p_1 peak, until stage coexistence is established (minimum in $|i|t^{1/2}$ vs $\log t$). Then, the x value that is achieved at steady state for this temperature is smaller than that obtained at 313 K or 296 K, so that a small amount of charge is inserted after the minimum. The lower x value reached and facile diffusion at low x concentration are probably the reasons why stage I is not formed inside graphite after p_2 at $T = 333$ K.

Exchange current density.—To get insight into the effect of temperature on the interphasial Li-ion flux, the exchange current density will be considered.

An Arrhenius-type plot, ln j_0 vs T^{-1}, is shown in Figure 12 for stages II (95 mV), I (50 mV), and Id (150 mV). In all cases, ln j_0 decreases linearly with T^{-1}, as observed in experimental data for the exchange current density[4,5] and the inverse of the charge transfer resistance,[8–10] with T^{-1}. j_0 becomes larger when temperature increases for all stages and thus particle flux across the interphase is faster, supporting the previous results obtained in CVs (Figure 3) and chronoamperometric transients (Figures 5, 8 and 10). For all temperatures, j_0 is bigger for stage II than for stages I and Id, as can be observed for room temperature in Figure S2 (Section S4) from the Supplementary Material.

Analysis of the slopes in the ln j_0 vs T^{-1} plots in Figure 12 shows that the formal activation energies for insertion/deinsertion, defined in Equation 3, are different for the various Li-ion occupations. These formal activation energy values are shown in Table III.

The largest activation energy corresponds to stage Id, the values for stages I and II being similar. This behavior can be understood as follows: observing the equilibrium isotherm for all temperatures it

Table III. Activation energy for charge transfer obtained from the Arrhenius plots of Figure 12 at different occupations conditions.

Stage	Electrode potential [mV]	Activation energy for charge transfer [eV]
Id	150	0.720 ± 0.003
II	95	0.679 ± 0.002
I	50	0.675 ± 0.001

becomes clear that Li-ion composition x at 150 mV differs slightly under different temperature conditions (Figure 13a), being the highest for 333 K, and the lowest for 296 K. Thus, the x value reached in a potentiostatic simulation when the system achieves the steady state, will be different for different temperatures. Under steady state conditions, the x value increases with temperature. Further, the interactions between inserted ions can be neglected at dilute Li composition. At the dilute Li-ion occupation achieved at 150 mV, the particle flux will therefore be higher for larger x values, and so will be the exchange current density. Consequently, a larger slope can be observed in the Arrhenius plot, as compared with stage II at 95 mV or stage I at 50 mV, where x is practically the same for all temperatures. The result is a higher sensitivity in the rate of charge transfer across the interphase to temperature at potentials where stage Id is formed, compared with the corresponding potentials of stage I and stage II.

From the literature we know that the slope of the $\ln j_0$ vs T^{-1} changes with electrolyte composition. Several articles have demonstrated that Li-ion desolvation from the electrolyte is the rate determining step for Li-ion insertion in graphite.[10,62] This means that changing $\Delta^*_{i/d}$ in simulations would emulate changes in electrolyte composition. kMC simulations with $\Delta^*_{i/d} = 0.655$ mV and $\Delta^*_{i/d} = 0.400$ mV representing changes in electrolyte composition are shown in Figure 13b where stage II is formed (95 mV). It is remarkable that the slopes found in the $\ln j_0$ vs T^{-1} plots resemble the input values used for $\Delta^*_{i/d}$. In fact, j_0 stems from the insertion/deletion of ions in a multiplicity of microscopic environments, which exhibit different activation energies as given by Equation 3. This encourages us to assume that the activation energy barriers found in experiments[5] are strongly representative of the microscopic situation. On the other hand, this means that it may be possible to emulate a change in the electrolyte composition by varying the energy barrier $\Delta^*_{i/d}$.

Table IV. Activation energy for diffusion, as obtained from the Arrhenius plots of Figure 14b at different Li-ion occupations conditions.

x	Activation energy for diffusion [eV]
0.00	0.370 ± 0.001
0.10	0.395 ± 0.002
0.21	0.53 ± 0.01
0.38	0.52 ± 0.04
0.52	0.21 ± 0.03
0.57	0.36 ± 0.07
0.80	0.471 ± 0.003
0.91	0.55 ± 0.04

Diffusion coefficients.—Having analyzed interfacial phenomena, it is pertinent now to focus on the Li-ion diffusion phenomenon inside graphite. $\log D_{ch}$ vs x plots are shown for different temperatures (Figure 14a). There, it is found that the $\log D_{ch}$ vs x plots have the same behavior as that described by Levi et al.:[24] the diffusion coefficients have maximum values for compositions corresponding to pure stages and to $x \to 0$. Furthermore, the D_{ch} values increase monotonically with temperature for all x. This behavior has been observed in the literature for similar temperature windows.[2,20,29]

Besides qualitative characterization, we can calculate the activation energies with the aid of Arrhenius plots (Figure 14b), as performed above with the exchange current density. The activation energy values for different lithium compositions, as obtained with the linear fits of Figure 14b, are shown in Table IV.

As an overall result, we can state that at low and high occupations the activation energy for diffusion evaluated from Figure 14b remains relatively constant, with a drop at intermediate occupations. This behavior can be ascribed to the easy transport of lithium in the mostly unoccupied planes at $x = 0.5$, where stage II is formed (c.f. Figure 9d). This trend agrees with the model of Persson et al., using effective cluster interactions obtained from DFT calculations.[17] A more quantitative statement requires performing simulations within a wider temperature range and will be addressed in future work.

Concerning experiments, the activation energy for diffusion obtained by Ecker et al.[4] for 15% graphite state of charge ($x = 0.15$) was 0.49 eV using galvanostatic the intermittent titration technique

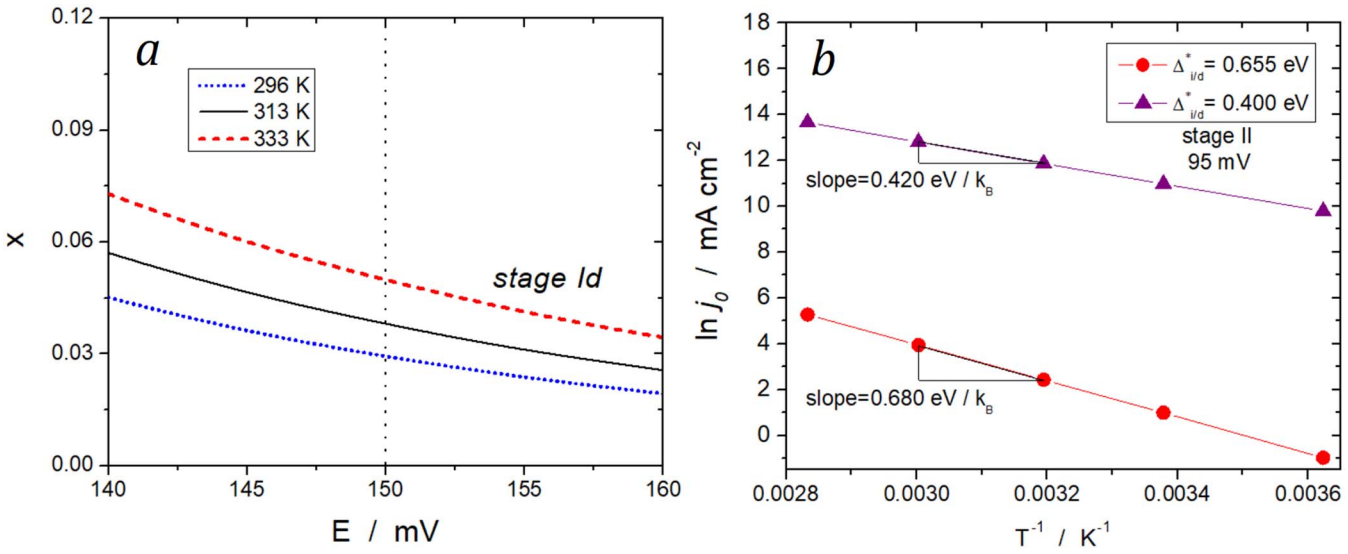

Figure 13. a) Occupation by lithium ions as a function of potential in a small potential window from Figure 6. The change of the occupation of stage Id with temperature can be appreciated. The potential used for the analysis of the activation energy of Stage Id is indicated with a vertical dotted line. b) Arrhenius plot for different activation barriers for the insertion/deinsertion process, $\Delta^*_{i/d}$. The lattice occupation corresponds to stage II and the exchange current densities were evaluated at 95 mV. The slopes of the linear fits are given in the plot. Error bars in Figure b are smaller than symbol size.

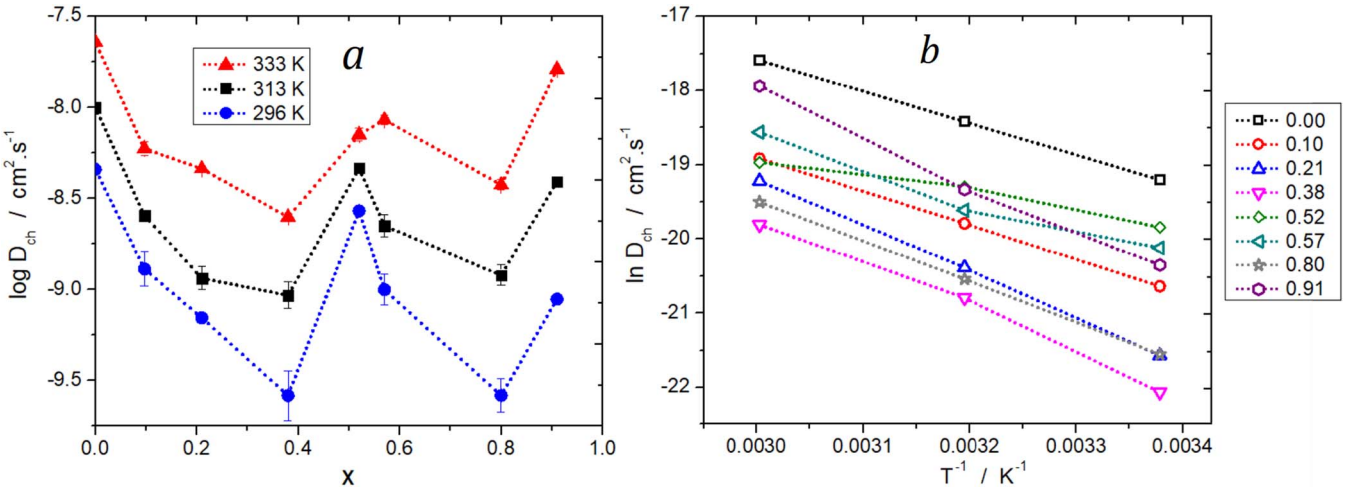

Figure 14. a) Chemical diffusion coefficients for different temperatures, calculated with Equation 4. b) Arrhenius plots for the diffusion coefficients obtained at different lithium composition, dotted lines are drawn to guide the eye.

(GITT) and 0.42 eV using electrochemical impedance spectroscopy (EIS). This value compares favorably with the theoretical value of $x = 0.21$ in Table IV. Kulova et al.[63] have calculated an activation energy of 0.36 eV for $x = 0.63$. This value is the same as that obtained with the present kMC simulations for $x = 0.57$ (Table IV). First-principles calculations for the full state of charge[13] report an activation energy barrier around 0.51 eV, a value close to that reported in Table IV for $x = 0.91$.

Conclusions

Within the present model and with the aid of kinetic Monte Carlo simulations we have analyzed the effect of temperature on cyclic voltammograms, potentiostatic steps and exchange current density for lithium-ion insertion in graphite. The features of cyclic voltammograms compared qualitatively well with experimental data from the literature, yielding an overview of temperature dependent lithium-ion insertion/deinsertion phenomena. Potentiostatic steps were also simulated at different temperatures, yielding two main components when the transients traversed potentials involving the coexistence of two phases. The peak p_1 occurring at shorter times, related to charge transfer processes across the interphase, was more strongly affected by temperature changes than the second peak than the second peak, p_2, by temperature changes, corresponding to slower diffusive processes. The two-component behavior agrees well with experiments conducted a room temperature and the present model allows predictions of behavior above room temperature.

The exchange current density was studied at different temperatures and different lithium-ion loadings of graphite. Our model suggests a linear behavior in Arrhenius-type plots of the logarithm of exchange current density with the reciprocal of temperature, as found in experiment. Changes in solvent composition were emulated by changing the insertion/deinsertion energy barrier. Our results suggest a relationship between the slope of the Arrhenius plot and the input variable of the barrier height, both of which yielded the same value of energy. This was a surprising finding given the multiplicity of possible microscopic environments for Li-ion ion exchange, since our model accounts for local interactions between Li ions.

Diffusion coefficients were calculated dependent on temperature and lithiation amount, x. We explained the experimentally observed trends in diffusion coefficients in terms of activation energies for different lithium compositions. These activation energies were determined from the trends in diffusion coefficients as a function of temperature dependent at these lithium-ion compositions.

Within our simulation methodology, two tasks remain: the first is the improvement of our computer code to perform simulations for larger systems, closer to the microscale. This may provide a more direct comparison with experimental studies of commercial graphite particles. However, as highlighted earlier, the present simulations could allow a direct comparison with more ideal electrode geometries which have recently become experimentally accessible.[60]

The second issue to address is the improvement of the interaction potentials to describe other stages of order >2 for lithium insertion in graphite. Recently, Mercer et al.[64] have been able to theoretically reproduce a peak and sharp change in potential that occurs for the insertion/deinsertion of Li^+ into/from graphite in the dilute Li^+ occupation limit. This improvement will be introduced in the kMC scheme in future studies.

Acknowledgments

M.P. Mercer and H.E. Hoster thank the Faraday Institution (faraday.ac.uk; EP/S003053/1), grant number FIRG003, for funding. E. M. Gavilán-Arriazu and O.A. Pinto thank Universidad Nacional de Santiago del Estero under project CICyT-UNSE 23/A242, Argentina, these authors also acknowledge the financial support received from CONICET PIP 11220130100547CO and CONICET PIO 14520140100013CO. E.P.M. Leiva acknowledges grants PIP CONICET 11220150100624CO, PUE/2017 CONICET, FONCYT PICT-2015-1605 and SECyT of the Universidad Nacional de Córdoba. Support by CCAD-UNC and GPGPU Computing Group, Y-TEC and an IPAC grant from SNCAD-MinCyT, Argentina, are also gratefully acknowledged.

ORCID

E. M. Gavilán-Arriazu https://orcid.org/0000-0002-5889-9659
M. P. Mercer https://orcid.org/0000-0001-7578-3554
O. A. Pinto https://orcid.org/0000-0001-9562-0496
O. A. Oviedo https://orcid.org/0000-0003-0738-9760
H. E. Hoster https://orcid.org/0000-0001-6379-5275
E. P. M. Leiva https://orcid.org/0000-0002-5557-6328

References

1. J. R. Dahn, Phase diagram of LixC6, *Phys. Rev. B.*, **44**, 9179 (1991).
2. M. D. Levi, C. Wang, D. Aurbach, and Z. Chvoj, Effect of temperature on the kinetics and thermodynamics of electrochemical insertion of Li-ions into a graphite electrode, *J. Electroanal. Chem.*, **562**, 187 (2004).
3. A. J. Bard and L. R. Faulkner, Electrochemical Methods : Fundamentals and Applications, 2001.
4. M. Ecker, T. K. D. Tran, P. Dechent, S. Käbitz, A. Warnecke, and D. U. Sauera, Parameterization of a physico-chemical model of a lithium-ion battery: I. Determination of parameters, *J. Electrochem. Soc.*, **162**, A1836 (2015).

5. M. C. Smart and B. V. Ratnakumar, Effects of electrolyte composition on lithium plating in lithium-ion cells, *J. Electrochem. Soc.*, **158**, 379 (2011).
6. Y. Chang, J. Jong, and G. T. Fey, Kinetic Characterization of the Electrochemical Intercalation of Lithium Ions into Graphite Electrodes, *J. Electrochem. Soc.*, **147**, 2033 (2000).
7. T. Piao, S. Park, C. Doh, and S. Moon, Intercalation of Lithium Ions into Graphite Electrodes Studied by AC Impedance Measurements, *J. Electrochem. Soc.*, **146**, 2794 (1999).
8. T. Abe, H. Fukuda, Y. Iriyama, and Z. Ogumi, Solvated Li-Ion Transfer at Interface Between Graphite and Electrolyte, *J. Electrochem. Soc.*, **151**, 1120 (2004).
9. Y. Yamada, Y. Iriyama, T. Abe, and Z. Ogumi, Kinetics of Lithium Ion Transfer at the Interface between Graphite and Liquid Electrolytes : Effects of Solvent and Surface Film, *Langmuir*., **25**, 12766 (2009).
10. K. Xu, A. Von Cresce, and U. Lee, Differentiating Contributions to " Ion Transfer " Barrier from Interphasial Resistance and Li þ Desolvation at Electrolyte / Graphite Interface, *Langmuir*., **26**, 11538 (2010).
11. H. Yang, H. J. Bang, and J. Prakash, Evaluation of Electrochemical Interface Area and Lithium Diffusion Coefficient for a Composite Graphite Anode, *J. Electrochem. Soc.*, **151**, 8 (2004).
12. X. Wang and K. Aoki, Transition of current of lithium intercalation from solution to graphite, *J. Electroanal. Chem.*, **604**, 101 (2007).
13. K. Toyoura, Y. Koyama, A. Kuwabara, F. Oba, and I. Tanaka, First-principles approach to chemical diffusion of lithium atoms in a graphite intercalation compound, *Phys. Rev. B.*, **78**, 1 (2008).
14. K. Toyoura, Y. Koyama, A. Kuwabara, and I. Tanaka, Effects of Off-Stoichiometry of LiC 6 on the Lithium Diffusion Mechanism and Diffusivity by First Principles Calculations, *J. Phys. Chem. C.*, **114**, 2375 (2010).
15. X. C. Tang, C. Y. Pan, L. P. He, L. Q. Li, and Z. Z. Chen, A novel technique based on the ratio of potentio-charge capacity to galvano-charge capacity (RPG) for determination of the diffusion coefficient of intercalary species within insertion-host materials: Theories and experiments, *Electrochim. Acta.*, **49**, 3113 (2004).
16. K. Persson, V. A. Sethuraman, L. J. Hardwick, Y. Hinuma, Y. S. Meng, A. Van Der Ven, V. Srinivasan, R. Kostecki, and G. Ceder, Lithium Diffusion in Graphitic Carbon, *J. Phys. Chem. Lett.*, **1**, 1176 (2010).
17. K. Persson, Y. Hinuma, Y. Meng, A. Van der Ven, and G. Ceder, Thermodynamic and kinetic properties of the Li-graphite system from first-principles calculations, *Phys. Rev. B.*, **82**, 1 (2010).
18. R. Kobayashi, N. Ohba, T. Tamura, and S. Ogata, A Monte Carlo study of host-material deformation effect on Li migration in graphite, *J. Phys. Soc. Japan.*, **82**, 1 (2013).
19. E. G. Leggesse, C. L. Chen, and J. C. Jiang, Lithium diffusion in graphene and graphite: Effect of edge morphology, Carbon N. Y., **103**, 209 (2016).
20. M. A. Cabañero, N. Boaretto, M. Röder, J. Müller, J. Kallo, and A. Latz, Direct determination of diffusion coefficients in commercial Li-ion batteries, *J. Electrochem. Soc.*, **165**, A847 (2018).
21. B. P. Freiländer, P. Heitjans, H. Ackermann, G. Kiese, H. Stöckmann, and C. Van Der Marel, Diffusion Processes in LiC6 Studied by B-NMR *, *Zeitschrift Für Phys. Chemie Neue Folge.*, **101**, 93 (1987).
22. J. Schmalstieg, C. Rahe, M. Ecker, and D. U. Sauer, Full cell parameterization of a high-power lithium-ion battery for a physico-chemical model: Part I. Physical and electrochemical parameters, *J. Electrochem. Soc.*, **165**, A3799 (2018).
23. A. Magerl, H. Zabel, and I. S. Anderson, In-plane jump diffusion of Li in LiC6, *Phys. Rev. Lett.*, **55**, 222 (1985).
24. M. D. Levi and D. Aurbach, Diffusion coefficients of lithium ions during intercalation into graphite derived from the simultaneous measurements and modeling of electrochemical impedance and potentiostatic intermittent titration characteristics of thin graphite electrodes, *J. Phys. Chem. B.*, **101**, 4641 (1997).
25. W. Lehnert and W. Schmickler, The diffusion of lithium through graphite : a Monte Carlo simulation based on electronic structure, *Chem. Phys.*, **163**, 331 (1992).
26. A. Mańquez and P. B. Balbuena, Molecular Dynamics Study of Graphite/Electrolyte Interfaces, *J. Electrochem. Soc.*, **148**, A624 (2001).
27. P. Yu, B. N. Popov, J. A. Ritter, and R. E. White, Determination of the Lithium Ion Diffusion Coefficient in Graphite, *J. Electrochem. Soc.*, **146**, 8 (1999).
28. H. Jun Guo, X. Hai Li, X. Ming Zhang, H. Qiang Wang, Z. Xing Wang, and W. Jie Peng, Diffusion coefficient of lithium in artificial graphite, mesocarbon microbeads, and disordered carbon, *New Carbon Mater.*, **22**, 7 (2007).
29. T. L. Kulova, A. M. Skundin, E. A. Nizhnikovskii, and A. V. Fesenko, Temperature effect on the lithium diffusion rate in graphite, *Russ. J. Electrochem.*, **42**, 259 (2006).
30. K. A. Fichthorn and W. H. Weinberg, Theoretical Foundations of Dynamic Monte-Carlo Simulations, *J. Chem. Phys.*, **95**, 1090 (1991).
31. S. Krishnan, G. Brenet, E. Machado-charry, D. Caliste, L. Genovese, T. Deutsch, and P. Pochet, Revisiting the domain model for lithium intercalated graphite, *Appl. Phys. Lett.*, **103**, 251904 (2014).
32. R. N. Methekar, P. W. C. Northrop, K. Chen, R. D. Braatz, and V. R. Subramanian, Kinetic Monte Carlo Simulation of Surface Heterogeneity in Graphite Anodes for Lithium-Ion Batteries: Passive Layer Formation, *J. Electrochem. Soc.*, **158**, A363 (2011).
33. M. D. Levi and D. Aurbach, The mechanism of lithium intercalation in graphite film electrodes in aprotic media. Part 1. High resolution slow scan rate cyclic voltammetric studies and modeling, *J. Electroanal. Chem.*, **421**, 79 (1997).
34. M. Chandesris, D. Caliste, D. Jamet, and P. Pochet, Thermodynamics and Related Kinetics of Staging in Intercalation Compounds, *J. Phys. Chem. C.*, **123**, 23711 (2019).
35. R. B. Smith, E. Khoo, and M. Z. Bazant, Intercalation Kinetics in Multiphase-Layered Materials, *J. Phys. Chem. C.*, **121**, 12505 (2017).
36. Y. Guo, R. B. Smith, Z. Yu, D. K. Efetov, J. Wang, P. Kim, M. Z. Bazant, and L. E. Brus, Li Intercalation into Graphite: Direct Optical Imaging and Cahn-Hilliard Reaction Dynamics, *J. Phys. Chem. Lett.*, **7**, 2151 (2016).
37. A. A. Franco, A. Rucci, D. Brandell, C. Frayret, M. Gaberscek, P. Jankowski, and P. Johansson, Boosting Rechargeable Batteries R&D by Multiscale Modeling: Myth or Reality?, *Chem. Rev.*, **119**, 4569 (2019).
38. Y. Yin, R. Zhao, Y. Deng, and A. A. Franco, Compactness of the Lithium Peroxide Thin Film Formed in Li-O2 Batteries and Its Link to the Charge Transport Mechanism: Insights from Stochastic Simulations, *J. Phys. Chem. Lett.*, **8**, 599 (2017).
39. F. Röder, R. D. Braatz, and U. Krewer, Direct coupling of continuum and kinetic Monte Carlo models for multiscale simulation of electrochemical systems, *Comput. Chem. Eng.*, **121**, 722 (2019).
40. F. Röder, R. D. Braatz, and U. Krewer, Multi-scale simulation of heterogeneous surface film growth mechanisms in lithium-ion batteries, *J. Electrochem. Soc.*, **164**, E3335 (2017).
41. E. M. Gavilán-Arriazu, O. A. Pinto, B. A. López De Mishima, D. E. Barraco, O. A. Oviedo, and E. P. M. Leiva, Kinetic Monte Carlo applied to the electrochemical study of the Li-ion graphite system, *Electrochim. Acta*, **331**, 135439 (2020).
42. C. Montella, Discussion of the potential step method for the determination of the diffusion coefficients of guest species in host materials, *J. Electroanal. Chem.*, **518**, 61 (2002).
43. M. D. Levi, E. Markevich, and D. Aurbach, The Effect of Slow Interfacial Kinetics on the Chronoamperometric Response of Composite Lithiated Graphite Electrodes and on the Calculation of the Chemical Diffusion Coefficient of Li Ions in Graphite, *J. Phys. Chem. B.*, **109**, 7420 (2005).
44. M. D. Levi, E. Markevich, and D. Aurbach, Comparison between Cottrell diffusion and moving boundary models for determination of the chemical diffusion coefficients in ion-insertion electrodes, *Electrochim. Acta.*, **51**, 98 (2005).
45. E. M. Gavilán-Arriazu, O. A. Pinto, B. A. López de Mishima, D. E. Barraco, O. A. Oviedo, and E. P. M. Leiva, The kinetic origin of the Daumas-Hérold model for the Li-ion/graphite intercalation system, *Electrochem. Commun.*, **93**, 133 (2018).
46. N. Daumas and A. Hérold, Notes des Membres et Correspontants et Notes Présentéesou Transmises par Leurs Soins, *C. R. Acad. Sci. Ser. C.*, **268**, 373 (1969).
47. M. Maiza, Y. Mammeri, D. A. Nguyen, N. Legrand, P. Desprez, and A. A. Franco, Evaluating the impact of transport inertia on the electrochemical response of lithium ion battery single particle models, *J. Power Sources.*, **423**, 263 (2019).
48. Y. Xin, A. Huang, Q. Hu, H. Shi, M. Wang, Z. Xiao, X. Zheng, Z. Di, and P. K. Chu, Barrier Reduction of Lithium Ion Tunneling through Graphene with Hybrid Defects : First-Principles Calculations, *Adv. Theory Simulations.*, **1**, 1700009 (2018).
49. P. A. Derosa and P. B. Balbuena, A Lattice-Gas Model Study of Lithium Intercalation in Graphite, *J. Electrochem. Soc.*, **146**, 3630 (1999).
50. E. M. Gavilán-Arriazu, O. A. Pinto, B. A. L. de Mishima, E. P. M. Leiva, and O. A. Oviedo, Grand Canonical Monte Carlo Study of Li Intercalation into Graphite, *J. Electrochem. Soc.*, **165**, A2019 (2018).
51. E. M. Gavilán Arriazu, B. A. López de Mishima, O. A. Oviedo, E. P. M. Leiva, and O. A. Pinto, Criticality of the phase transition on stage two in a lattice-gas model of a graphite anode in a lithium-ion battery, *Phys. Chem. Chem. Phys.*, **19**, 23138 (2017).
52. E. M. Perassi and E. P. M. Leiva, A theoretical model to determine intercalation entropy and enthalpy: Application to lithium/graphite, *Electrochem. Commun.*, **65**, 48 (2016).
53. D. P. DiVincenzo and E. J. Mele, Self-consistent effective-mass theory for intralayer screening in graphite intercalation compounds, *Phys. Rev. B.*, **29**, 1685 (1984).
54. S. J. Mitchell, G. Brown, and P. A. Rikvold, Dynamics of Br electrosorption on single-crystal Ag(100): A computational study, *J. Electroanal. Chem.*, **493**, 68 (2000).
55. G. Brown, P. A. Rikvold, M. A. Novotny, and A. Wieckowski, Simulated Dynamics of Underpotential Deposition of Cu with Sulfate on Au(111), *J. Electrochem. Soc.*, **146**, 1035 (1999).
56. A. F. Voter, Introduction to The Kinetic Monte Carlo Method, in: K.E. Sickafus, E.A. Kotomin, and B.P. Uberuaga, (Eds.), *Radiat. Eff. Solids, Springe*, pp. 1 (2007).
57. N. Metropolis, A. W. Rosenbluth, M. N. Rosenbluth, A. H. Teller, and E. Teller, Equation of state calculations by fast computing machines, *J. Chem. Phys.*, **21**, 1087 (1953).
58. S. A. Paz and E. P. M. Leiva, Time recovery for a complex process using accelerated dynamics, *J. Chem. Theory Comput.*, **11**, 1725 (2015).
59. C. Uebing and R. Gomer, A Monte Carlo study of surface diffusion coefficients in the presence of adsorbate–adsorbate interactions. I. Repulsive interactions, *J. Chem. Phys.*, **95**, 7626 (1991).
60. B. Tao, L. C. Yule, E. Daviddi, C. L. Bentley, and P. R. Unwin, Correlative Electrochemical Microscopy of Li-Ion (De)intercalation at a Series of Individual LiMn2O4 Particles, *Angew. Chemie - Int. Ed.*, **58**, 4606 (2019).
61. B. Markovsky, M. D. Levi, and D. Aurbach, The basic electroanalytical behavior of practical graphite–lithium intercalation electrodes, *Electrochim. Acta.*, **43**, 2287 (1998).
62. T. R. Jow, S. A. Delp, J. L. Allen, J.-P. Jones, and M. C. Smart, Factors Limiting Li^+ Charge Transfer Kinetics in Li-Ion Batteries, *J. Electrochem. Soc.*, **165**, A361 (2018).
63. T. L. Kulova and A. M. Skundin, Balance between Reversible and Irreversible Processes during Lithium Intercalation in Graphite, *Russ. J. Electrochem.*, **42**, 292 (2006).
64. M. P. Mercer, M. Otero, M. Ferrer-Huerta, A. Sigal, D. E. Barraco, H. E. Hoster, and E. P. M. Leiva, Transitions of lithium occupation in graphite: A physically informed model in the dilute lithium occupation limit supported by electrochemical and thermodynamic measurements, *Electrochim. Acta.*, **324**, 134774 (2019).